Science Advances
AAAS

advances.sciencemag.org/cgi/content/full/6/29/eaba0509/DC1

Supplementary Materials for

Helicity-dependent photocurrents in the chiral Weyl semimetal RhSi

Dylan Rees, Kaustuv Manna, Baozhu Lu, Takahiro Morimoto, Horst Borrmann, Claudia Felser, J. E. Moore, Darius H. Torchinsky*, J. Orenstein*

*Corresponding author. Email: dtorchin@temple.edu (D.H.T.); jworenstein@lbl.gov (J.O.)

Published 15 July 2020, *Sci. Adv.* **6**, eaba0509 (2020)
DOI: 10.1126/sciadv.aba0509

This PDF file includes:

Supplementary Text

Crystal Growth and Structure Refinement

Single crystals of RhSi were grown from a melt using the vertical Bridgman crystal growth technique. Here the crystal growth was performed with an off-stoichiometric composition with slightly excess Si. First, a polycrystalline ingot was prepared using the arc melt technique with the stoichiometric mixture of Rh and Si metal pieces of 99.99 % purity. Then the crushed powder was filled in a custom-designed sharp-edged alumina tube and finally sealed inside a tantalum tube with argon atmosphere. The temperature profile for the crystal growth was controlled with a thermocouple attached at the bottom of the tantalum ampoule containing the sample. The sample was heated to 1500°C and then slowly cooled to cold zone with a rate of 0.8 mm/h. Single crystals with average dimension of $\sim$15 mm length and $\sim$6 mm diameter were obtained. A picture of the grown crystal is shown in the inset of Fig. S1. The crystals were analyzed with a white beam backscattering Laue X-ray diffraction technique at room temperature. The samples show very sharp spots that can be indexed by a single pattern, revealing excellent quality of the grown crystals without any twinning or domains. A Laue diffraction pattern of the oriented RhSi single crystal superposed with a theoretically simulated pattern is presented in Fig. S1. The structural parameters were determined using a Rigaku AFC7 four-circle diffractometer with a Saturn 724+ CCD-detector applying graphite-monochromatized Mo-Kα radiation. The crystal structure was refined to be cubic $P2_13$ (#198) with lattice parameter, a=4.6858(9) Å.

Material Symmetries

1. Nonlinear Tensor in the [111] basis

The second-order optical nonlinearity generates currents at both the sum and difference frequencies of the applied electric field. LPGE and CPGE correspond to the current generated at

the difference frequency,

$$j_i \propto \sigma_{ijk} E_j E_k^* \tag{1}$$

For cubic space group $P2_13$ the only nonvanishing elements of σ_{ijk} have indices xyz and permutations. The elements with even permutations of xyz are equal to σ_{xyz} and odd permutations are equal to σ^*_{xyz}. If we write $\sigma_{xyz} = \alpha + i\gamma$ where α and γ are both real, the structure of the third rank tensor can be displayed in the form,

$$\sigma^{(2)} = \begin{pmatrix} \begin{pmatrix} 0 \\ 0 \\ 0 \end{pmatrix} & \begin{pmatrix} 0 \\ 0 \\ \alpha + i\gamma \end{pmatrix} & \begin{pmatrix} 0 \\ \alpha - i\gamma \\ 0 \end{pmatrix} \\ \begin{pmatrix} 0 \\ 0 \\ \alpha - i\gamma \end{pmatrix} & \begin{pmatrix} 0 \\ 0 \\ 0 \end{pmatrix} & \begin{pmatrix} \alpha + i\gamma \\ 0 \\ 0 \end{pmatrix} \\ \begin{pmatrix} 0 \\ \alpha + i\gamma \\ 0 \end{pmatrix} & \begin{pmatrix} \alpha - i\gamma \\ 0 \\ 0 \end{pmatrix} & \begin{pmatrix} 0 \\ 0 \\ 0 \end{pmatrix} \end{pmatrix} \tag{2}$$

where the element σ_{ijk} is the kth element of the column vector in the ith row and jth column of the matrix.

2. Transformation properties of the CPGE

The circular photogalvanic current can be written in terms of the photon helicity,

$$j_i \propto \beta_{ij} (\mathbf{E} \times \mathbf{E}^*)_j. \tag{3}$$

The second rank CPGE tensor is contracted from the third-rank conductivity tensor according to the relation,

$$\beta_{ij} = \sigma_{ikl} \epsilon_{jkl}, \tag{4}$$

where ϵ_{jkl} is the unit antisymmetric tensor. Substitution of the conductivity tensor for the RhSi space group (Eq. 2) yields,

$$\beta_{ij} = i\beta\delta_{ij}, \tag{5}$$

where δ_{ij} is the Kronecker delta. Substitution into Eq. 3 yields,

$$\mathbf{j} \propto i\beta \mathbf{E} \times \mathbf{E}^*, \tag{6}$$

which shows that for the case of space group $P2_13$ the CPGE current is always directed parallel to the helicity vector, regardless of its direction with respect to the crystal axes.

3. LPGE sample rotation dependence

We use Rodrigues' rotation formula to transform this tensor into the basis where z' is parallel to the [111] direction in the crystal basis, which yields

$$\sigma^{(2)} \propto \begin{pmatrix} \begin{pmatrix} -\alpha\sqrt{2} \\ 0 \\ -1 \end{pmatrix} & \begin{pmatrix} 0 \\ \alpha\sqrt{2} \\ i\gamma\sqrt{3} \end{pmatrix} & \begin{pmatrix} -\alpha \\ -i\gamma\sqrt{3} \\ 0 \end{pmatrix} \\ \begin{pmatrix} 0 \\ \alpha\sqrt{2} \\ -i\gamma\sqrt{3} \end{pmatrix} & \begin{pmatrix} \alpha\sqrt{2} \\ 0 \\ -\alpha \end{pmatrix} & \begin{pmatrix} \sqrt{3}\alpha \\ -\alpha \\ 0 \end{pmatrix} \\ \begin{pmatrix} -\alpha \\ i\gamma\sqrt{3} \\ 0 \end{pmatrix} & \begin{pmatrix} -\sqrt{3}\alpha \\ -\alpha \\ 0 \end{pmatrix} & \begin{pmatrix} 0 \\ 0 \\ 2\alpha \end{pmatrix} \end{pmatrix}. \tag{7}$$

Using this tensor we can calculate the LPGE response for fixed linear pump polarization as the crystal is rotated about the z' (or [111]) axis. The crystal rotation corresponds to the transformation $\sigma'_{\alpha\beta\gamma} = R_{\alpha i}(\phi)R_{\beta j}(\phi)R_{\gamma k}(\phi)\sigma_{ijk}$, where,

$$R(\phi) = \begin{pmatrix} \cos(\phi) & \sin(\phi) & 0 \\ -\sin(\phi) & \cos(\phi) & 0 \\ 0 & 0 & 1 \end{pmatrix}. \tag{8}$$

If, for example, the pump polarization is fixed in the x' direction, then the LPGE current depends only on the tensor elements σ'_{xxx} and σ'_{yxx} and from Eqs. 7 and 8 we have,

$$\begin{aligned} \sigma'_{xxx} &= R_{xx}^3\sigma_{xxx} + R_{xx}R_{xy}^2\sigma_{xyy} + R_{xy}R_{xx}R_{xy}\sigma_{yxy} + R_{xy}^2R_{xx}\sigma_{yyx} \\ &\propto \left(-\sqrt{2}\cos^3(\phi) + 3\sqrt{2}\cos\phi\sin^2\phi\right) \\ &= -\sqrt{2}\cos(3\phi) \end{aligned} \tag{9}$$

and

$$\begin{aligned}\sigma'_{yxx} = R_{yx}R_{xx}^2\sigma_{yxy} + R_{yx}R_{xy}^2\sigma_{xyy} + R_{yy}R_{xx}R_{xy}\sigma_{yxy} + R_{yy}R_{xy}R_{xx}\sigma_{yyx} \\ \propto \left(-3\sqrt{2}\cos^2\phi\sin\phi - \sqrt{2}\sin^3\phi\right) \\ = \sqrt{2}\sin(3\phi).\end{aligned} \tag{10}$$

From Eqs. 9 and 10 we obtain the dependence of the LPGE current on crystal rotation angle,

$$\mathbf{j}(\phi) \propto \cos(3\phi)\hat{\mathbf{x}}' - \sin(3\phi)\hat{\mathbf{y}}'. \tag{11}$$

Eq. 11 implies that the angle, θ, of the LPGE current relative to the x' axis is given by $\theta = 3\phi$. This is consistent with what is observed and shown in Fig. 2C and 2D in the main text.

Material Properties

1. Linear optical properties

We performed reflectivity measurements in the range .08eV - 3eV (main text, Fig. 4A) and used Kramers-Kronig analysis to compute the complex index of refraction $\tilde{n} = n + i\kappa$. This and the complex dielectric permittivity $\tilde{\epsilon} = \tilde{n}^2$ are plotted in Fig S2. We additionally calculate $\sigma_1 = 2n\kappa\epsilon_0\omega$ (main text Fig. 4B and Fig. S2A) along with α, t_s, t_p and θ_{in} (Fig. S4A-C) which are the absorption coefficient, Fresnel transmission coefficients and the angle of refraction for 45° angle of incidence. These are defined by

$$\begin{aligned}\theta_{in} &= \arcsin\frac{\sin\theta_i}{n} \\ \alpha &= \frac{2\omega\kappa}{c} \\ t_s &= \frac{2\cos\theta_i}{\cos\theta_i + \tilde{n}\cos\theta_{in}} \\ t_p &= \frac{2\cos\theta_i}{\tilde{n}\cos\theta_i + \cos\theta_{in}}\end{aligned} \tag{12}$$

where $\theta_i = 45^\circ$ is the angle of incidence of the pump light.

We compare the predicted optical conductivity of the Γ and R nodes in RhSi with our measured σ_1 in Fig. S3A and Fig. 4B in the main text. The fraction of the total optical conductivity that represents the predicted linear conductivity is shown in Fig. S3B.

2. Scattering time (τ)

Using the measured value of σ_{dc}, we infer the equillibrium scattering time to be $\tau = 8.6$ fs from our results for $\sigma_1(\omega)$ using the form for the Drude conductivity

$$\sigma_1(\omega) = \frac{\sigma_{dc}}{1 + \omega^2\tau^2}. \tag{13}$$

3. Terahertz index of refraction

The complex index of refraction at THz frequencies determines the impedance mismatch between RhSi and free space. We can obtain an accurate estimate of $\tilde{n}$ from the dc conductivity. Given the value of τ determined in the previous section, the THz emission lies in the low frequency limit of the optical conductivity, where $\omega\tau \ll 1$ and $\sigma(\omega) \to \sigma_{dc}$. In this regime, the complex permittivity at low frequency is

$$\tilde{\epsilon}(\omega) = -\frac{\tilde{\sigma}(\omega)}{i\omega} = \frac{i\sigma_{dc}}{\omega}. \tag{14}$$

The complex index of refraction is then given as,

$$\tilde{n} \equiv n + i\kappa = \sqrt{\frac{\tilde{\epsilon}(\omega)}{\epsilon_0}} = (1+i)\sqrt{\frac{\sigma_{dc}}{2\epsilon_0\omega}} \tag{15}$$

which at 1 THz is equal to $57(1 + i)$. Although our Kramers-Kronig analysis begins to become somewhat unreliable for photon energies less than $\sim$10meV, it agrees with our analysis and gives $\tilde{n}(1\text{THz}) = 51 + 57i$, confirming that Eq. 15 is correct. When calculating $\beta\tau$ in our analysis, we use $\tilde{n}(\omega)$ to find the frequency dependent transmission of the THz radiation from RhSi into free space.

4. Inferring laser pulse length from emitted THz radiation

It is not feasible using conventional methods such as autocorrelation to characterize the pulse length T of the laser over the entire wavelength range. Lacking a more precise method, we use the THz time traces to estimate the pulse length at each wavelength, since the laser does not necessarily produce the same pulse width across its available wavelength range. We know that the photocurrent scattering time τ is much shorter than the pulse length, which means that the instantaneous current follows the applied electric field squared. The effect of the OAP collection filters, described in a later section, which modify the spectrum of the terahertz radiation is to apply a second derivative to the pulse waveform, since for low frequencies the transmission function's leading term is ω^2. By making this approximation we find that the full width half maximum of the terahertz pulse t_1 is related to T by the equation

$$t_1 = \sqrt{\frac{1 - 2W(\sqrt{e}/4)}{2}}T \tag{16}$$

where $W(z)$ is the Lambert W function, or product log. This allows us to calculate an approximate pulse length for each wavelength. The results are presented in Fig. S4A.

Inferring the CPGE amplitude from the detected electro-optic signal

In this section we describe the normalization factors needed to convert from signal at the electro-optic detector to the CPGE saturation coefficient $\beta\tau$. This process involves the following three steps.

1. Determine the time-dependent electric field in the sample that arises from a photogenerated surface current which depends on laser parameters (intensity at the sample) and material parameters (β, τ, Fresnel coefficients, etc.).

2. Compute the Fourier transform of the terahertz pulse, the apply two filters to it. The first is the frequency-dependent transmission of the radiation into free space, $1/(\tilde{n}(\omega) + 1)$. The

second is the transfer function of the collection optics, $\mathcal{F}(\omega)$, that quantifies the fraction of radiation that is collected by the system and transferred to the ZnTe detection crystal.

3. Compute the inverse Fourier transform of the resulting spectrum, then convert the resulting time-dependent electric field at the ZnTe surface crystal to signal at the output of the biased photodetector scheme.

In order to obtain the value of $\beta\tau$ of RhSi, we assume $\beta = \beta_0 = \pi e^3/3h^2$ and $\tau = 1$ fs for all pump frequencies in this calculation. Then, by dividing the amplitude of the measured signal to the expected signal given all experimental parameters, we yield a value for $\beta\tau$ at each pump frequency in units of ($\beta_0 \times$fs).

1. Calculation of the radiated field from the sample

Assume we have some CPGE coefficient β. For circularly polarized light, CPGE is given by

$$\frac{dj}{dt} = \beta |E|^2. \tag{17}$$

As laser light travels through a material at angle θ_{in} relative to the normal direction z, its intensity decays according to the (power) attenuation coefficient along the direction of propagation, $r_k = z/\cos\theta_{in}$:

$$|E|^2 = E_0^2 e_k^{-\alpha r_k}. \tag{18}$$

The sheet current density generation rate is then given by

$$\begin{aligned} \frac{dK}{dt} &= \int_0^\infty dz \frac{dj}{dt} \sin\theta_{in} \\ &= \beta E_0^2 \sin\theta_{in} \int_0^\infty dz e_k^{-\alpha z/\cos\theta_{in}} \\ &= \beta \frac{1}{2\alpha} E_0^2 \sin 2\theta_{in} \end{aligned} \tag{19}$$

and the saturation current density is

$$K = \beta\tau \frac{1}{2\alpha} E_0^2 \sin 2\theta_{in}. \tag{20}$$

The factor of $\sin\theta_{in}$ represents the fraction of the current parallel to the surface, which is what radiates into free space. Since the scattering rate τ is much less than the pulse length T, the current amplitude follows the electric field squared amplitude and will radiate in the THz regime. The radiated electric field amplitude can be found as follows. From Ampère's law we have

$$\begin{aligned} E\tfrac{\tilde{n}}{c} = B = \tfrac{\mu_0}{2}K \\ \implies E = \tfrac{\mu_0 c}{2\tilde{n}}K. \end{aligned} \tag{21}$$

Using the Fresnel transmission coefficient $t = 2\tilde{n}/(\tilde{n}+1)$, the external radiation is given by

$$E_{ext} = \frac{\mu_0 c}{2\tilde{n}}Kt = \frac{Z_0}{\tilde{n}+1}K. \tag{22}$$

Using Eq. 20 we get

$$E_{ext}^{THz} = \frac{\beta Z_0 \tau}{2\alpha(\tilde{n}+1)}E_0^2 \sin 2\theta_{in}. \tag{23}$$

The frequency dependence of the factor $1/(\tilde{n}(\omega)+1)$ is shown in Fig. S5A. Now we must express E_0 in terms of the measured laser parameters average power P, repetition rate f, spot size r_0 and pulse duration T. At normal incidence the intensity of the electric field of the pump laser at the surface of the sample is given by

$$I(r,t) = \frac{c\epsilon_0}{2}E^2(r,t) = \frac{c\epsilon_0}{2}E_{\text{ext}}^2 e^{-r^2/r_0^2}e^{-t^2/T^2} \tag{24}$$

Integrating over space and time yields the relation

$$E_{\text{ext}}^2 = \frac{2PZ_0}{\pi\sqrt{\pi}fTr_0^2}, \tag{25}$$

where we include a factor of 1/2 to account for 45° angle of incidence. This leaves us with a peak THz electric field of

$$E_{ext}^{THZ} = \frac{Z_0^2\beta\tau t_s t_p P \sin 2\theta_{in}}{\pi\sqrt{\pi}\alpha f T r_0^2(\tilde{n}+1)} \tag{26}$$

which radiates into free space and eventually is detected through electrooptic sampling. In order to experimentally determine the spectrum of $\beta\tau$, each of the terms in the above equation must

be determined as a function of the pump frequency. As discussed earlier, we calculate t_s, t_p, $\theta_{in} = \arcsin 1/(\sqrt{2}n)$ and $\alpha = 2\kappa\omega/c$ as a function of pump frequency based on spectrally resolved reflectivity measurements and Kramers-Kronig analysis which produces the complex index of refraction. These values are plotted in Fig. S3C-D. The laser power P is directly measured across the laser's spectral range. We use a concave focal length $F = 50$ cm mirror to focus light on the sample, gives a focused spot size of $r_0 = \frac{2F\lambda}{\pi d}$ where d is the collimated beam diameter.

2. Radiation from the photoexcited region

The THz radiation emitted by the sample is collected by a 45° OAP which collimates the beam. A second OAP then focuses it onto a ZnTe electro-optic sampling (EOS) crystal. In order to calculate the fraction of radiated light collected by the OAP, we start with the formula for the vector potential at location $\mathbf{r}$ from a current density described by $\mathbf{j}(\mathbf{r}, t)$,

$$\mathbf{A}(\mathbf{r}, t) = \frac{\mu_0}{4\pi} \int d^3\mathbf{r}' \frac{\mathbf{j}\left(\mathbf{r}, t_r\right)}{|\mathbf{r} - \mathbf{r}'|} \tag{27}$$

where t_r is the retarded time. If we assume for the moment radiation at a specific frequency ω, the current density in our experiment is given by

$$\mathbf{j}\left(\mathbf{r}, t\right) = J_0 \hat{x} \delta(z) e^{-x^2/2r_0^2} e^{-y^2/r_0^2} e^{-(t - x' \sin\theta_i/c)^2/T^2} \tag{28}$$

where the term $x' \sin\theta_i/c$ in the final exponential represents the phase delay across the photoexcited spot due to off-normal incidence at angle $\theta_i = 45^\circ$ (Fig. S6A). The coordinates used in the calculation are shown in Fig. S6B.

The retarded time at $\mathbf{r}$ is given by

$$\begin{aligned} t_r &= t - |\mathbf{r} - \mathbf{r}'|/c \\ &= t - \frac{1}{c}\sqrt{r^2 - 2\mathbf{r}\cdot\mathbf{r}' + r'^2} \\ &\approx t - \frac{1}{c} r\left(1 - \hat{\mathbf{r}}\cdot\mathbf{r}'/r\right) \\ &= t - \frac{r}{c} + \frac{\hat{\mathbf{r}}\cdot\mathbf{r}'}{c} \\ &= t - \frac{r}{c} + \frac{1}{c}\left(\sin\theta\cos\phi x' + \sin\theta\sin\phi y'\right). \end{aligned} \tag{29}$$

where the OAP is in the far field limit $r' \ll r$.

The Fourier transform of the vector potential is

$$\mathbf{A}(\mathbf{r},\omega) = \frac{\mu_0}{4\pi r} j_0 \hat{x} \int dt e^{i\omega t} \int dx' dy' e^{-\frac{x^2}{2r_0^2}} e^{-\frac{y^2}{r_0^2}} e^{-u^2/T^2} \tag{30}$$

where $u = t_r - \frac{x'\sin\theta_i}{c} = t - \frac{r}{c} + (\sin\theta\cos\phi - \sin\theta_i)\frac{x'}{c} + \sin\theta\sin\phi\frac{y'}{c}$. This gives

$$\begin{aligned} \mathbf{A}(\mathbf{r},\omega) = \frac{\mu_0}{4\pi r} j_0 \hat{x} e^{-\omega^2 T^2/4} e^{i\omega r/c} \int dx' e^{-\frac{x'^2}{2r_0^2}} e^{i\omega x'(\sin\theta\cos\phi - \sin\theta_i)/c} \\ \times \int dy' e^{-\frac{y'^2}{r_0^2}} e^{i\omega y'\sin\theta\sin\phi/c} \end{aligned} \tag{31}$$

$$= \frac{\mu_0}{4\sqrt{2}r} r_0^2 \sqrt{\pi} j_0 \hat{x} e^{-\omega^2 T^2/4} e^{i\omega r/c} e^{-\frac{r_0^2\omega^2}{2c^2}(\sin\theta_i - \sin\theta\cos\phi)^2} e^{-\frac{r_0^2\omega^2}{4c^2}\sin^2\theta\sin^2\phi} \tag{32}$$

The fraction of the total radiation captured by the OAP is given by

$$\mathcal{F}(\omega) = \int_{OAP} d\theta d\phi \sin\theta E(\omega,\theta,\phi) \Big/ \int_{2\pi} d\theta d\phi \sin\theta E(\omega,\theta,\phi). \tag{33}$$

The second integral is integrated over the upper half-sphere ($0 < \theta < \pi/2$) because we only consider the radiation emitted away from the sample, not into it. All θ- and ϕ-independent factors can be removed from the integrand, so we can use the form

$$E(\theta,\phi) \propto \cos\theta e^{-\frac{r_0^2\omega^2}{2c^2}(\sin\theta_i - \sin\theta\cos\phi)^2} e^{-\frac{r_0^2\omega^2}{4c^2}\sin^2\theta\sin^2\phi} \tag{34}$$

in the integrand. The integral depends on spot size, r_0, which is variable across the spectral range of the pump laser. We calculate this integral numerically for each pump wavelength.

$\mathcal{F}(\omega)$ is plotted for several pump wavelengths in Fig. S5B as a function of $\nu = \omega/2\pi$. For small wavelengths relative to the excitation spot size, the radiation emits at the specular direction relative to the incoming pump light.

3. Electro-optic detection using ZnTe

The last step in the calibration is the conversion of the electric field at the surface of the ZnTe crystal to the signal at the output of the biased photodetector scheme. Detection of the THz field is performed through electro-optic sampling (EOS) in ZnTe (110). In this technique the THz electric field induces transient birefringence, Δn, in the ZnTe, which is detected by a co-propagating probe beam at 800 nm. Our analysis is based on the detailed studies of the EOS in technique presented in Refs. (***?***, ***?***). For THz frequencies below 3 THz we neglect dispersion in ZnTe and assume a real index $n = 2.85$ (***?***).

The transient birefringence generates a polarization rotation in the probe beam. We measure the rotation using an optical bias scheme (***?***, ***?***) that yields a gain factor of 88 as compared with the conventional balanced detector measurement. In the conventional scheme, the fractional change in the balanced output is given by,

$$\frac{\Delta V(\tau)}{V} = \frac{\omega n^3 r_{41}}{2c} \int_0^L dz \int_{-\infty}^{\infty} dt E_{THz}(z,t) I_0(z, t-\tau) \tag{35}$$

where ω is the angular frequency of the probe pulse, c is the speed of light, L is the propagation distance through the crystal, E_{THz} is the THz field strength, $r_{41} = 4$ pm/V is the electro-optic coefficient of ZnTe at 800 nm, $n = 2.85$ is the index of refraction of ZnTe and

$$I_0(z, t-\tau) = I_0 \exp\{-[z - v_g(t-\tau)]^2/(v_g T_{pr})^2\} \tag{36}$$

is the normalized intensity of the 800 nm probe beam with pulse duration, T_{pr}, which propagates with group velocity v_g.

THz transients with bandwidth less than 3 THz, Eq. 35 simplifies to,

$$\frac{\Delta V(\tau)}{V} = \frac{\omega n^3 r_{41} L}{2c} \int_{-\infty}^{\infty} dt E_{THz}(t) I_0(t-\tau). \tag{37}$$

Because the duration of the probe pulse is approximately 35 fs, much less that the time scale of the THz transient, we make the approximation that $I_0(t-\tau) \rightarrow \delta(t-\tau)$ to obtain (*?*)

$$\frac{\Delta V(\tau)}{V} = \frac{\omega n^3 r_{41} L}{2c} E_{THz}(\tau). \tag{38}$$

An additional factor of $2/(n+1)$ is needed because the THz field is partially reflected at the surface of the ZnTe. Finally, we substitute E_{THz} with the expression in Eq. 26 (after applying the frequency dependent collection filters) and as discussed earlier set $\beta\tau = \beta_0 \times 1$fs. This gives an expected EOS signal for each pump frequency based on laser parameters, material properties and the experimental geometry, and by comparing the measured value with the expected value we obtain $\beta\tau$ in units of ($\beta_0 \times$fs). The results are plotted in the main text in Fig. 3.

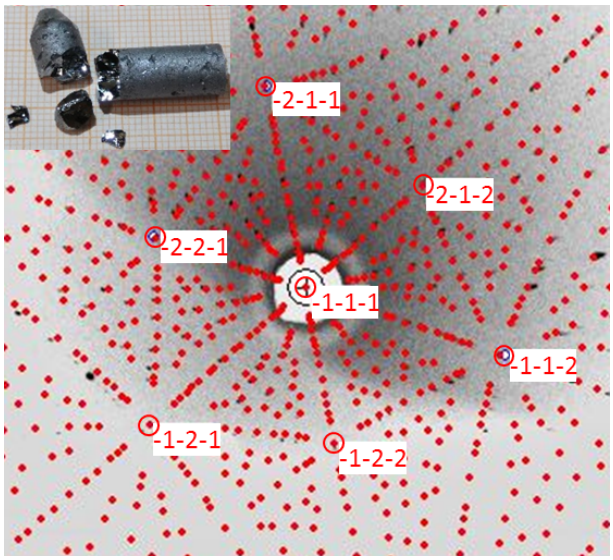

Fig. S1. Crystal growth and diffraction. Laue diffraction pattern of a [111] oriented RhSi single crystal superposed with a theoretically simulated pattern. Inset shows picture of the grown RhSi single crystal. Photo credit: Kaustuv Manna, Max Planck Institute for Chemical Physics of Solids.

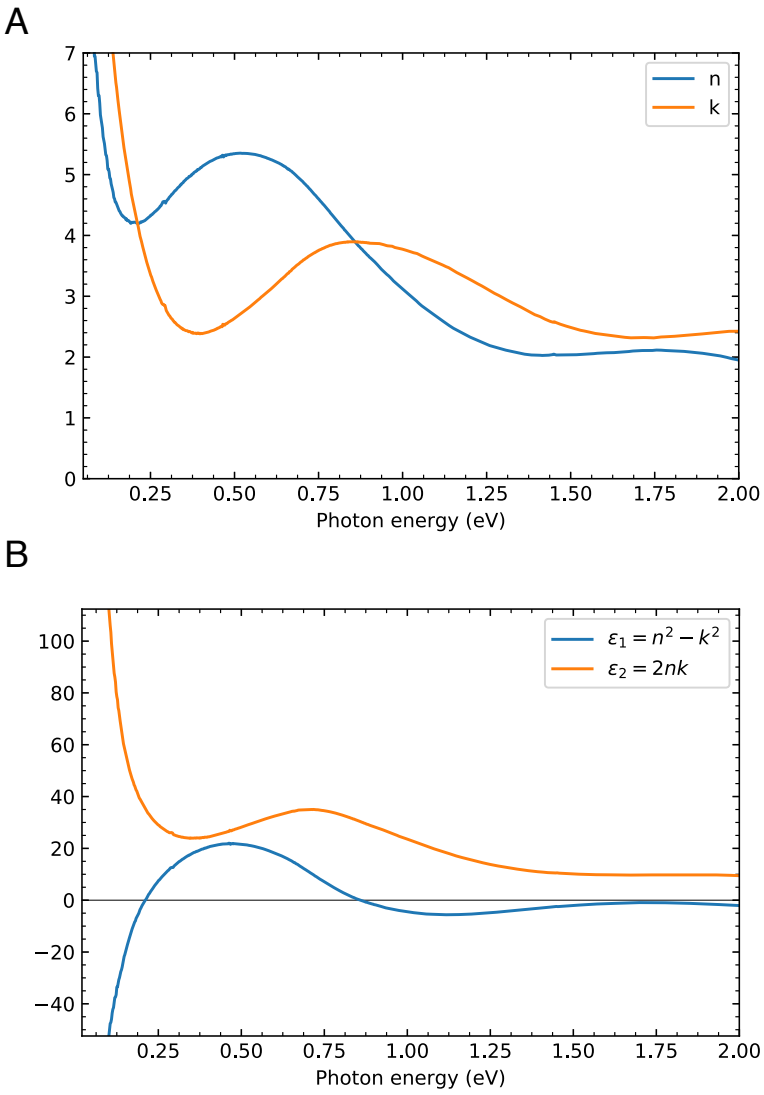

Fig. S2. Material properties. (**A**) The real and imaginary parts of the refractive index. (**B**) The real and imaginary parts of the complex dielectric function.

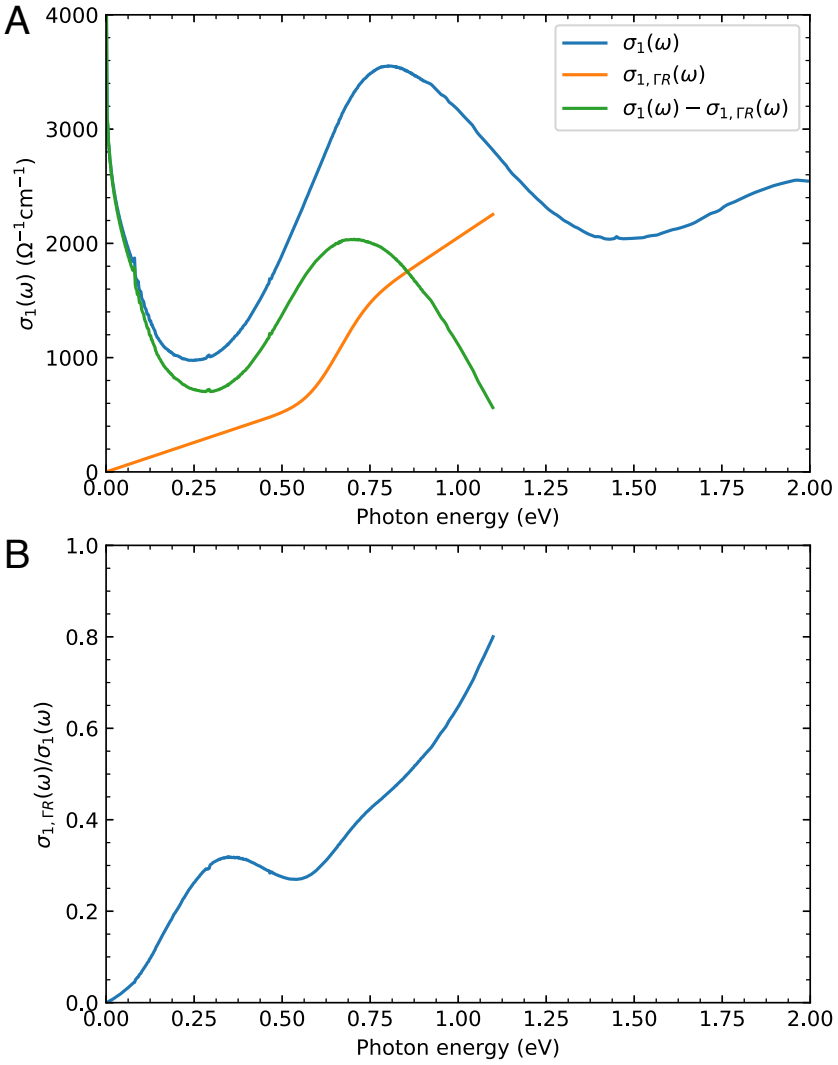

Fig. S3. Ideal conductivity. (**A**) Here we compare the ideal Γ and R band conductivity, $\sigma_{1,\Gamma R}$, with the total conductivity of RhSi, σ_1. (**B**) The fraction of σ_1 which constitutes the ideal Weyl conductivity.

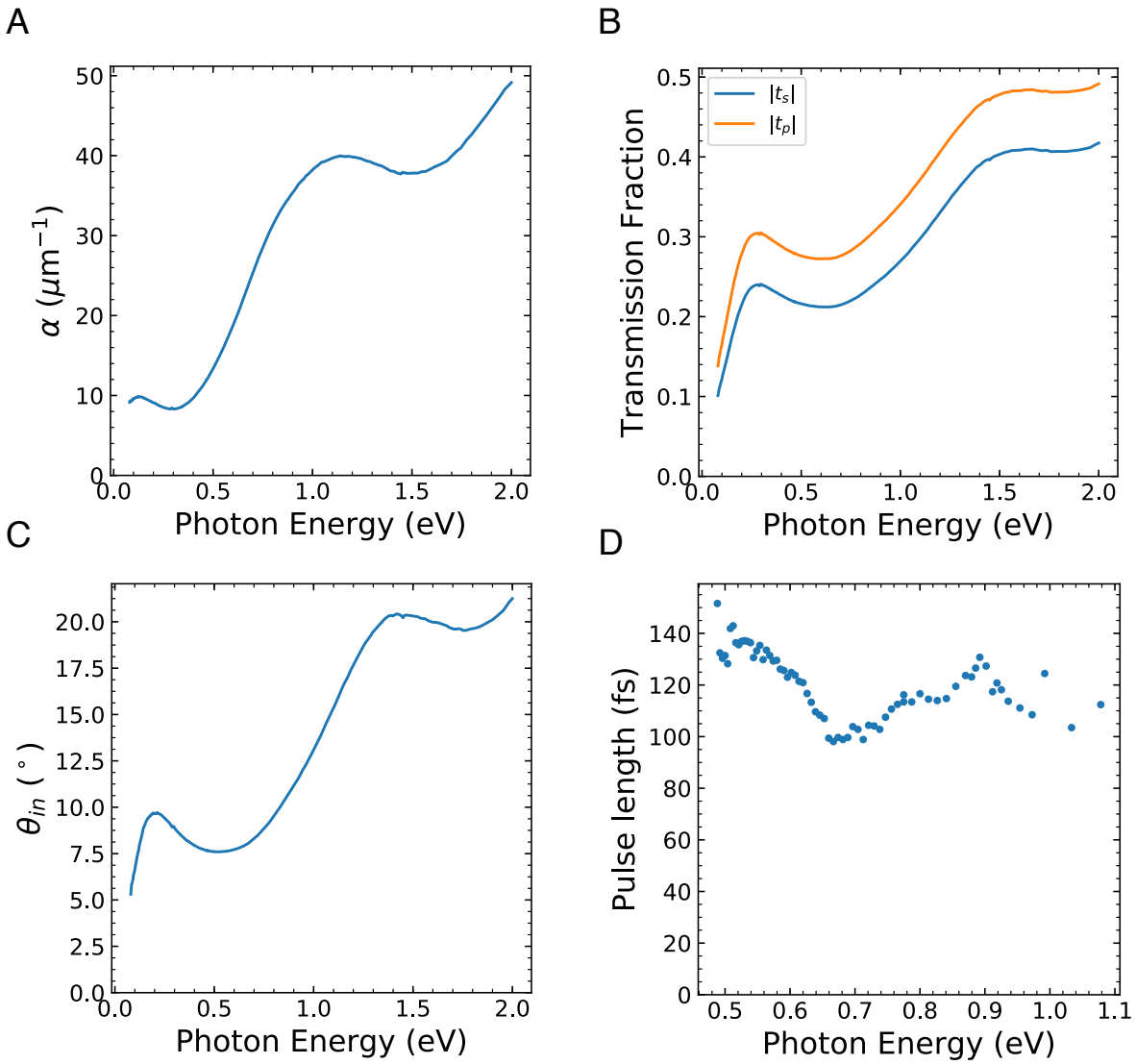

Fig. S4. Material properties. (**A**) Power absorption coefficient α. (**B**) Fresnel transmission coefficient magnitudes $|t_s|$ and $|t_p|$. (**C**) Angle of refraction for incident angle $\theta_i = 45°$. (**D**) Pump pulse length T estimated from the emitted terahertz waveforms.

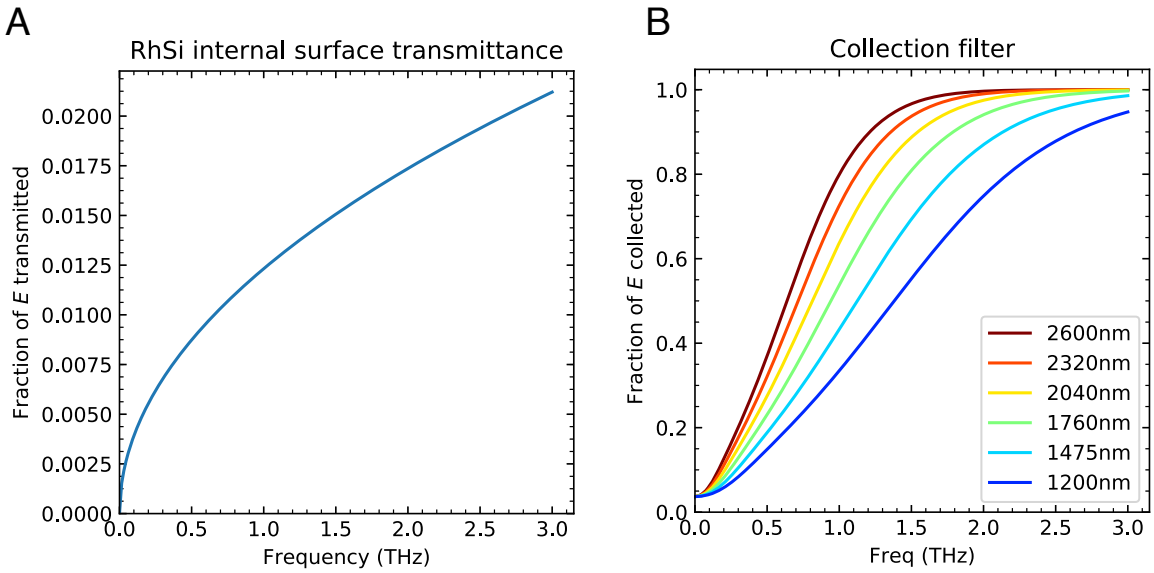

Fig. S5. Surface THz transmission and collection filter. (**A**) Fraction of terahertz radiation transmitted from bulk into free space, determined by dc conductivity and optical conductivity measurements. (**B**) Fraction of terahertz collected and collimated by the OAP.

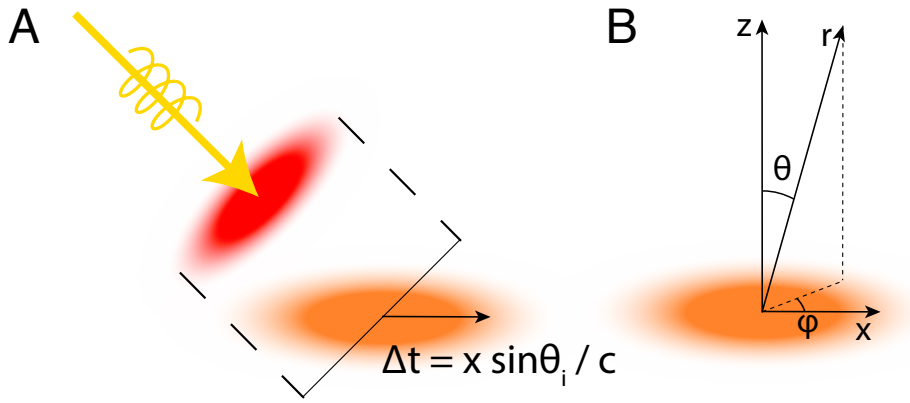

Fig. S6. Filter calculation geometry (**A**) Illustration of photoexcited current at off-normal incidence. The pump light (red shading) is cast onto the sample which excites a current (orange shading). There is a time delay across the photoexcited region which affects the radiated angle, as in a phased array antenna. (**B**) Illustration of the polar coordinate system used in the filter calculation.

REFERENCES AND NOTES

1. H. Weyl, Elektron und gravitation. I. *Zeitschrift für Physik* **56**, 330–352 (1929).
2. N. P. Armitage, E. J. Mele, A. Vishwanath, Weyl and Dirac semimetals in three-dimensional solids. *Rev. Mod. Phys.* **90**, 015001 (2018).
3. H. B. Nielsen, M. Ninomiya, The Adler-Bell-Jackiw anomaly and Weyl fermions in a crystal. *Phys. Lett. B* **130**, 389–396 (1983).
4. X. Wan, A. M. Turner, A. Vishwanath, S. Y. Savrasov, Topological semimetal and Fermi-arc surface states in the electronic structure of pyrochlore iridates. *Phys. Rev. B* **83**, 205101 (2011).
5. S.-Y. Xu, C. Liu, S. K. Kushwaha, R. Sankar, J. W. Krizan, I. Belopolski, M. Neupane, G. Bian, N. Alidoust, T.-R. Chang, H.-T. Jeng, C.-Y. Huang, W.-F. Tsai, H. Lin, P. P. Shibayev, F.-C. Chou, R. J. Cava, M. Z. Hasan, Observation of Fermi arc surface states in a topological metal. *Science* **347**, 294–298 (2015).
6. B. Q. Lv, H. M. Weng, B. B. Fu, X. P. Wang, H. Miao, J. Ma, P. Richard, X. C. Huang, L. X. Zhao, G. F. Chen, Z. Fang, X. Dai, T. Qian, H. Ding, Experimental discovery of Weyl semimetal TaAs. *Phys. Rev. X* **5**, 031013 (2015).
7. S.-Y. Xu, I. Belopolski, N. Alidoust, M. Neupane, G. Bian, C. Zhang, R. Sankar, G. Chang, Z. Yuan, C.-C. Lee, S.-M. Huang, H. Zheng, J. Ma, D. S. Sanchez, B. Wang, A. Bansil, F. Chou, P. P. Shibayev, H. Lin, S. Jia, M. Z. Hasan, Discovery of a Weyl fermion semimetal and topological Fermi arcs. *Science* **349**, 613–617 (2015).
8. S.-Y. Xu, N. Alidoust, I. Belopolski, Z. Yuan, G. Bian, T.-R. Chang, H. Zheng, V. N. Strocov, D. S. Sanchez, G. Chang, C. Zhang, D. Mou, Y. Wu, L. Huang, C.-C. Lee, S.-M. Huang, B. Wang, A. Bansil, H.-T. Jeng, T. Neupert, A. Kaminski, H. Lin, S. Jia, M. Zahid Hasan, Discovery of a Weyl fermion state with Fermi arcs in niobium arsenide. *Nat. Phys.* **11**, 748–754 (2015).
9. M. Z. Hasan, S.-Y. Xu, I. Belopolski, S.-M. Huang, Discovery of Weyl fermion semimetals and topological Fermi arc states. *Annu. Rev. Condens. Matter Phys.* **8**, 289–309 (2017).
10. V. I. Belinicher, B. I. Sturman, The photogalvanic effect in media lacking a center of symmetry. *Sov. Phys. Uspekhi* **23**, 199–223 (1980).

11. V. M. Asnin, A. A. Bakun, A. M. Danishevskii, E. L. Ivchenko, G. E. Pikus, A. A. Rogachev, “Circular” • photogalvanic effect in optically active crystals. *Solid State Commun.* **30**, 565–570 (1979).
12. E. L. Ivchenko, G. E. Pikus, Photogalvanic effects in optically active crystals. *Ferroelectrics* **43**, 131–136 (1982).
13. S. D. Ganichev, V. V. Bel’kov, P. Schneider, E. L. Ivchenko, S. A. Tarasenko, W. Wegscheider, D. Weiss, D. Schuh, E. V. Beregulin, W. Prettl, Resonant inversion of the circular photogalvanic effect in *n*-doped quantum wells. *Phys. Rev. B* **68**, 035319 (2003).
14. S. D. Ganichev, W. Prettl, Spin photocurrents in quantum wells. *J. Phys. Condens. Matter* **15**, R935–R983 (2003).
15. P. Hosur, Circular photogalvanic effect on topological insulator surfaces: Berry-curvature-dependent response. *Phys. Rev. B* **83**, 035309 (2011).
16. H. Plank, J. Pernul, S. Gebert, S. N. Danilov, J. König-Otto, S. Winnerl, M. Lanius, J. Kampmeier, G. Mussler, I. Aguilera, D. Grützmacher, S. D. Ganichev, Infrared/terahertz spectra of the photogalvanic effect in (Bi,Sb)Te based three-dimensional topological insulators. *Phys. Rev. Materials* **2**, 024202 (2018).
17. F. de Juan, A. G. Grushin, T. Morimoto, J. E. Moore, Quantized circular photogalvanic effect in Weyl semimetals. *Nat. Commun.* **8**, 15995 (2017).
18. Q. Ma, S.-Y. Xu, C.-K. Chan, C.-L. Zhang, G. Chang, Y. Lin, W. Xie, T. Palacios, H. Lin, S. Jia, P. A. Lee, P. Jarillo-Herrero, N. Gedik, Direct optical detection of Weyl fermion chirality in a topological semimetal. *Nat. Phys.* **13**, 842 (2017).
19. K. Sun, S.-S. Sun, L.-L. Wei, C. Guo, H.-F. Tian, G.-F. Chen, H.-X. Yang, J.-Q. Li, Circular photogalvanic effect in the Weyl semimetal TaAs. *Chin. Phys. Lett.* **34**, 117203 (2017).
20. N. Sirica, R. I. Tobey, L. X. Zhao, G. F. Chen, B. Xu, R. Yang, B. Shen, D. A. Yarotski, P. Bowlan, S. A. Trugman, J.-X. Zhu, Y. M. Dai, A. K. Azad, N. Ni, X. G. Qiu, A. J. Taylor, R. P. Prasankumar, Tracking ultrafast photocurrents in the Weyl semimetal TaAs using THz emission spectroscopy. *Phys. Rev. Lett.* **122**, 197401 (2019).
21. Y. Gao, Y. Qin, Y. P. Liu, Y. L. Su, S. Kaushik, E. J. Philip, X. Chen, Z. Li, H. Weng, D. E. Kharzeev, M. K. Liu, J. Qi, Coherent terahertz emission with tunable ellipticity and optical chirality from the Weyl semimetal TaAs. *Nat. Commun.* **11**, 720 (2020).

22. Z. Ji, G. Liu, Z. Addison, W. Liu, P. Yu, H. Gao, Z. Liu, A. M. Rappe, C. L. Kane, E. J. Mele, R. Agarwal, Spatially dispersive circular photogalvanic effect in a Weyl semimetal. *Nat. Mater.* **18**, 955–962 (2019).
23. J. Ma, Q. Gu, Y. Liu, J. Lai, P. Yu, X. Zhuo, Z. Liu, J.-H. Chen, J. Feng, D. Sun, Nonlinear photoresponse of type-II Weyl semimetals. *Nat. Mater.* **18**, 476–481 (2019).
24. C.-K. Chan, N. H. Lindner, G. Refael, P. A. Lee, Photocurrents in weyl semimetals. *Phys. Rev. B* **95**, 041104 (2017).
25. G. Chang, B. J. Wieder, F. Schindler, D. S. Sanchez, I. Belopolski, S.-M. Huang, B. Singh, D. Wu, T.-R. Chang, T. Neupert, S.-Y. Xu, H. Lin, M. Z. Hasan, Topological quantum properties of chiral crystals. *Nat. Mater.* **17**, 978–985 (2018).
26. B. Bradlyn, J. Cano, Z. Wang, M. G. Vergniory, C. Felser, R. J. Cava, B. A. Bernevig, Beyond dirac and weyl fermions: Unconventional quasiparticles in conventional crystals. *Science* **353**, aaf5037 (2016).
27. G. Chang, S.-Y. Xu, B. J. Wieder, D. S. Sanchez, S.-M. Huang, I. Belopolski, T.-R. Chang, S. Zhang, A. Bansil, H. Lin, M. Z. Hasan, Unconventional chiral fermions and large topological Fermi arcs in RhSi. *Phys. Rev. Lett.* **119**, 206401 (2017).
28. P. Tang, Q. Zhou, S.-C. Zhang, Multiple types of topological fermions in transition metal silicides. *Phys. Rev. Lett.* **119**, 206402 (2017).
29. F. Flicker, F. de Juan, B. Bradlyn, T. Morimoto, M. G. Vergniory, A. G. Grushin, Chiral optical response of multifold fermions. *Phys. Rev. B* **98**, 155145 (2018).
30. F. de Juan, Y. Zhang, T. Morimoto, Y. Sun, J. E. Moore, A. G. Grushin, Difference frequency generation in topological semimetals. *Phys. Rev. Res.* **2**, 012017 (2020).
31. D. S. Sanchez, I. Belopolski, T. A. Cochran, X. Xu, J.-X. Yin, G. Chang, W. Xie, K. Manna, V. Süß, C.-Y. Huang, N. Alidoust, D. Multer, S. S. Zhang, N. Shumiya, X. Wang, G.-Q. Wang, T.-R. Chang, C. Felser, S.-Y. Xu, S. Jia, H. Lin, M. Z. Hasan, Topological chiral crystals with helicoid-arc quantum states. *Nature* **567**, 500–505 (2019).
32. D. Takane, Z. Wang, S. Souma, K. Nakayama, T. Nakamura, H. Oinuma, Y. Nakata, H. Iwasawa, C. Cacho, T. Kim, K. Horiba, H. Kumigashira, T. Takahashi, Y. Ando, T. Sato, Observation of chiral fermions with a large topological charge and associated Fermi-arc surface states in CoSi. *Phys. Rev. Lett.* **122**, 076402. (2019).

33. N. B. Schröter, D. Pei, M. G. Vergniory, Y. Sun, K. Manna, F. de Juan, J. A. Krieger, V. Süss, M. Schmidt, P. Dudin, B. Bradlyn, T. K. Kim, T. Schmitt, C. Cacho, C. Felser, V. N. Strocov, Y. Chen, Chiral topological semimetal with multifold band crossings and long Fermi arcs. *Nat. Phys.* **15**, 759–765 (2019).
34. M.-A. Sánchez-Martínez, F. de Juan, A. G. Grushin, Linear optical conductivity of chiral multifold fermions. *Phys. Rev. B* **99**, 155145 (2019).
35. L. Z. Maulana, K. Manna, E. Uykur, C. Felser, M. Dressel, A. V. Pronin, Optical conductivity of multifold fermions: The case of RhSi. *Phys. Rev. Res.* **2**, 023018 (2020).
36. H. J. Bakker, G. C. Cho, H. Kurz, Q. Wu, X.-C. Zhang, Distortion of terahertz pulses in electro-optic sampling. *J. Opt. Soc. Am. B* **15**, 1795–1801 (1998).
37. G. Gallot, D. Grischkowsky, Electro-optic detection of terahertz radiation. *J. Opt. Soc. Am. B* **16**, 1204–1212 (1999).
38. A. Nahata, A. S. Weling, T. F. Heinz, A wideband coherent terahertz spectroscopy system using optical rectification and electro-optic sampling. *Appl. Phys. Lett.* **69**, 2321–2323 (1996).
39. F. D. J. Brunner, J. A. Johnson, S. Grübel, A. Ferrer, S. L. Johnson, T. Feurer, Distortion-free enhancement of terahertz signals measured by electro-optic sampling. I. Theory. *J. Opt. Soc. Am. B* **31**, 904–910 (2014).
40. J. A. Johnson, F. D. J. Brunner, S. Grübel, A. Ferrer, S. L. Johnson, T. Feurer, Distortion-free enhancement of terahertz signals measured by electro-optic sampling. II. Experiment. *J. Opt. Soc. Am. B* **31**, 1035–1040 (2014).